IN-34

13485

P22

Characteristics of 3D Turbulent Jets in Crossflow

A. O. Demuren
Institute for Computational Mechanics in Propulsion
Lewis Research Center
Cleveland, Ohio

NASA
LEWIS RESEARCH CENTER
ICOMP
CASE WESTERN
RESERVE UNIVERSITY

NASA

CHARACTERISTICS OF 3D TURBULENT JETS IN CROSSFLOW

A. O. Demuren*
Institute for Computational Mechanics in Propulsion
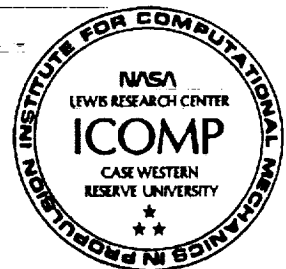Lewis Research Center
Cleveland, Ohio 44135

ABSTRACT

Three-dimensional turbulent jets in crossflow at low to medium jet-to-crossflow velocity ratios are computed with a finite-volume numerical procedure which utilizes a second-moment closure model to approximate the Reynolds stresses. A multigrid method is used to accelerate the convergence rate of the procedure. Comparison of the computations to measured data show good qualitative agreement. All trends are correctly predicted, though there is some uncertainty on the height of penetration of the jet. The evolution of the vorticity field is used to explore the jet–crossflow interaction.

INTRODUCTION

Three-dimensional turbulent jets in crossflow have important engineering applications in both confined and unconfined environments. Examples of jets issuing into confined crossflow include internal cooling of turbine blades, dilution air jets in combustion chambers, jets from V/STOL aircraft in transition flight, etc. The examples of turbulent jets issuing into unconfined (semi-infinite) crossflow include discharges from cooling towers or chimney stacks into the atmosphere, or of sewerage or waste heat into water bodies, film-cooling of turbine blades, etc. Several experimental investigations give insight into the various characteristics of the jet–crossflow interaction. The earlier studies typified by Kamotani and Greber [1] measured mostly global properties such as jet trajectory and spreading rates for a wide range of conditions. These results showed that the trajectory based on the temperature field often differed from the trajectory based on the velocity field. The same applies to the spread rates. There is thus some ambiguity as to what constitutes jet fluid as opposed to the jet boundaries and extent of mixing. Flow visualization studies by Foss[2] present an insight into the differences in flow regimes between lower and higher jet-to-crossflow velocity ratios, R. For the same configurations, measurements of the mean-flow and several higher order turbulent statistics are presented by Andreopoulos and Rodi[3] and Andreopoulos[4]. These constitute the most detailed set of measured data of jets-in-crossflow existing in the open literature. However, in regions with reverse flow, or high turbulence levels the accuracy of the data would not be very high. There is therefore still need for "accurate" numerical

1

computations in understanding the flow phenomena. Sykes et al [5] used a numerical method to explore the vorticity dynamics of jets in crossflow at high R. Their computations showed good qualitative agreement with the measured data [3] at R=2, except for turbulent kinetic energy levels, which were grossly overpredicted in the wake of the jet.

The present paper examines flow features at moderate R, using a finite-volume based multigrid method to compute the mean-flow and a second-moment closure model for the Reynolds stresses.

MATHEMATICAL MODEL

Mean-Flow

The time-averaged, three-dimensional, steady state equations governing the turbulent flow and heat/concentration transfer may be expressed in cartesian tensor notation as: Continuity

$$\frac{\partial}{\partial y^i}(\rho U_i) = 0 \tag{1}$$

Momentum

$$\frac{\partial}{\partial y^j}(\rho U_j U_i) = -\frac{\partial}{\partial y^i}P + \frac{\partial}{\partial y^j}\left[-\rho\overline{u_i u_j} + \mu\left(\frac{\partial U_i}{\partial y^j} + \frac{\partial U_j}{\partial y^i}\right)\right] \tag{2}$$

Temperature/Concentration

$$\frac{\partial}{\partial y^j}(\rho U_j \Phi) = S_\phi + \frac{\partial}{\partial y^j}\left[-\rho\overline{u_i \varphi} + \lambda\left(\frac{\partial \Phi}{\partial y^j}\right)\right] \tag{3}$$

with i=1,2,3 and j=1,2,3 representing properties in the lateral, vertical and longitudinal directions, respectively. y^j ($- y^1, y^2, y^3$) represents the cartesian coordinates; U_i the cartesian velocity components; P the pressure and Φ the normalized temperature or concentration. ρ is the density, μ is the molecular viscosity and λ is the thermal or species diffusivity. The equations are expanded by using Einstein's summation rule for repeated indices. $-\rho\overline{u_i u_j}$ and $-\rho\overline{u_i \varphi}$ are respectively, the Reynolds stresses and heat/concentration fluxes which must be determined by a turbulence model before the system of equations can be closed.

Turbulence Model

The transport equations for the Reynolds stresses may be expressed as:

$$\frac{\partial}{\partial y^j}(\rho U_j \overline{u_i u_j}) = \rho(d_{ij} + P_{ij} + \pi_{ij} - \epsilon_{ij}) \tag{4}$$

where the terms on the right hand side are respectively, diffusive transport, shear production, pressure-strain redistribution, and viscous dissipation. Of these, only the shear production can be represented exactly. All other terms must be modeled in order to close the system

of equations. Dissipation is modeled with the assumption of local isotropy of small scales to yield $\epsilon_{ij} = 2/3\epsilon\delta_{ij}$, where ϵ is the rate of dissipation of turbulent kinetic energy, $k(= \frac{1}{2}\overline{u_i u_i})$. Following Launder, Reece and Rodi [6], hereafter denoted LRR, we utilize a gradient diffusive transport model and a quasi-isotropic model for the pressure-strain. The resulting modeled equations may be written as:

$$\frac{\partial}{\partial y^j}(\rho U_j \overline{u_i u_j}) = \frac{\partial}{\partial y^m}(c_s \rho \frac{k}{\epsilon}\overline{u_m u_k}\frac{\partial \overline{u_i u_j}}{\partial y^k})$$

$$-\rho\{(1-\alpha)[\overline{u_i u_l}\frac{\partial U_l}{\partial y^j} + \overline{u_j u_l}\frac{\partial U_l}{\partial y^i}] - \beta[\overline{u_i u_l}\frac{\partial U_j}{\partial y^l} + \overline{u_j u_l}\frac{\partial U_i}{\partial y^l}]$$

$$+\frac{2}{3}\delta_{ij}(\alpha+\beta)\overline{u_k u_l}\frac{\partial U_l}{\partial y^k} + \gamma k(\frac{\partial U_j}{\partial y^i} + \frac{\partial U_i}{\partial y^j})$$

$$+\frac{c_1 \epsilon}{k}(\overline{u_i u_j} - \frac{2}{3}\delta_{ij}k) + \frac{2}{3}\delta_{ij}\epsilon\} \tag{5}$$

with the empirical coefficients $\alpha, \beta, \gamma, c_1$, and c_s given by:

$$\alpha = 0.7636 - 0.06 f; \ \beta = 0.1091 + 0.06 f; \ \gamma = 0.182;$$

$$c_1 = 1.5 - 0.50 f; \ c_s = 0.22$$

Wall-proximity effects are approximated with the function f which takes a value of unity near walls decreasing asymptotically to zero in a completely free stream (see Demuren and Rodi [7]). The distribution of ϵ is obtained from the solution to the modeled transport equation:

$$\frac{\partial}{\partial y^j}(\rho U_j \epsilon) = \frac{\partial}{\partial y^m}(c_\epsilon \rho \frac{k}{\epsilon}\overline{u_m u_k}\frac{\partial \epsilon}{\partial y^k}) + \frac{1}{2}\rho c_{\epsilon 1}P_{ii}\frac{\epsilon}{k} - c_{\epsilon 2}\rho\frac{\epsilon^2}{k} \tag{6}$$

Rather than solve the corresponding equations for the turbulent heat/concentration fluxes $\overline{u_i \varphi}$, we employ eddy-diffusivity relations as:

$$-\rho\overline{u_i \varphi} = \frac{\mu_t}{\sigma_\Phi}\frac{\partial \Phi}{\partial y^i} \tag{7}$$

μ_t is the eddy viscosity given by :

$$\mu_t = c_\mu \rho\frac{k^2}{\epsilon} \tag{8}$$

The empirical coefficients in Eq. (6)-(8) take values:

$$c_\epsilon = 0.15, \ c_\mu = 0.09, \ c_{\epsilon 1} = 1.44, \ c_{\epsilon 2} = 1.92, \ \sigma_t = 0.9$$

3

Boundary Conditions

Four types of boundary conditions are encountered, namely: inlet, outlet, symmetry and walls. Inlet conditions are specified from experimental data. The outlet is an outflow boundary requiring no formal specification of conditions. Along symmetry planes the normal gradients of all variables are set to zero, and the normal velocity component is also zero. The walls are special in that we do not integrate all the way down, rather we use the wall-function method [7] to prescribe the values of the dependent variables at the nodes immediately adjacent to the walls. The nodes are located such that the flow is in the fully turbulent region where the logarithmic law of the wall may be expected to apply. However, in the complex flow field under investigation here, this is unlikely to be the case everywhere. An improved wall-matching technique, such as that proposed by Degani and Walker[8] would probably be more appropriate. The flow which comes out of the jet hole is in general not uniform but is distorted to an extent which depends on R. At high R, there is very little distortion so uniform exit velocity may not be in much error. However, at low R (e.g. 0.5), Andreopoulos and Rodi [3] found that there was hardly any outflow through the front half near the stagnation point, and the vertical velocity near the lee side was measured to be more than 150 percent of the mean. The best way to treat this case is to solve for the flow within the discharge pipe as well, Demuren and Rodi[9] have found that the imposition of a constant total pressure at the discharge plane produced nearly the correct distribution of the vertical velocity. This approach is adopted here.

The boundary conditions for the turbulence quantities are prescribed along near-wall nodes based on the assumption of local equilibrium. Hence, we use the equation:

$$P_{ij} + \pi_{ij} - \epsilon_{ij} = 0 \qquad (9)$$

which is effectively an algebraic stress model. Further, the assumption of the logarithmic law of the wall enables the values of k and ϵ at the near-wall nodes to be related to the friction velocity U_* as:

$$k_w = \frac{(U_*)^2}{\sqrt{c_\mu}} \; ; \; \epsilon_w = \frac{(U_*)^3}{\kappa y_w} \qquad (10)$$

where κ is the von Karman constant with value 0.42, and y_w is the normal distance from the wall to the respective node.

SOLUTION PROCEDURE

Equations (1)–(8) form a closed set which should be solved simultaneously to yield distributions of the mean-flow and turbulence quantities. The system of equations are discretized by a semi-implicit, finite-volume procedure based on the SIMPLE algorithm of Patankar and Spalding[10]. The original algorithm, as well as proposed improvements [11,12] have poor convergence properties, especially for three-dimensional recirculating flows. This deficiency is removed in the present work by a multigrid technique which uses SIMPLEC [11] merely as a relaxation (smoothing) scheme. Shaw et al [13] have shown that the SIMPLE algorithm

4

(or extensions thereof) has good smoothing properties. Details of the multigrid procedure are provided below. The semi-implicit method involves a linearization which decouples the system of equations because the full Jacobian matrices are not evaluated. Although this practice produces a scalar system of matrix equations which are computationally cheap to solve, the system may become stiff if large source terms have to be treated explicitly. Such a situation would arise if the Reynolds stresses in Eq. (2) have large gradients, as one might expect in the flows under consideration here. the consequence of that would be massive underrelaxation required to ensure stability with the attendant slow convergence rate. The stiffness can be reduced considerably by splitting the Reynolds stress $\overline{u_i u_j}$ into two parts:

$$\overline{u_i u_j} = \overline{u_i u_j}' - \frac{\mu_t}{\rho}\left(\frac{\partial U_i}{\partial y^j} + \frac{\partial U_j}{\partial y^i}\right) \tag{11}$$

The first part is treated explicitly. The second part is added to the molecular diffusion term and treated implicitly. The modified momentum equation has the form:

$$\frac{\partial}{\partial y^j}(\rho U_j U_i) = -\frac{\partial}{\partial y^i}P$$
$$+\frac{\partial}{\partial y^j}\left[-\rho\overline{u_i u_j}' + (\mu + \mu_t)\left(\frac{\partial U_i}{\partial y^j} + \frac{\partial U_j}{\partial y^i}\right)\right] \tag{12}$$

The resulting system of equations is now very stable and can be solved with standard iteration methods.

Multigrid Procedure

In the present work the FAS-FMG (full approximation storage-full multigrid) algorithm originally developed by Brandt [14] is employed to solve the hydrodynamic equations. The present implementation derives from previous works by Demuren [15] and Vanka [16]. There are however significant differences. First, the present method uses a regular grid system with no staggering of the velocity nodes relative to the pressure nodes. The expected odd-even decoupling problem is overcome by adding a fourth-order artificial dissipation term to the pressure gradient. It can be shown that, with a coefficient of unity, this practice is equivalent to the so-called "momentum interpolation" method of Peric [17]. However, there is now the flexibility to vary the coefficient all the way down to zero, if necessary. The second difference is that the system of equations is now solved in a sequential manner as opposed to the coupled approach proposed by Vanka. Numerical experiments showed no advantage in using the latter in a multigrid procedure, and it can be shown mathematically that it is less stable in a single-grid procedure. Further, the decoupled procedure is more easily vectorized.

The basic steps of the relaxation process are:

1. Solve the U_1 momentum equation using a guessed pressure field.

2. Then the U_2 momentum equation.

3. Then the U_3 momentum equation.

4. Compute the velocities on the faces of the control volume, each by linear interpolation plus a fourth-order artificial dissipation term.

5. Then compute the mass source error in each control volume.

6. Solve a pressure-correction equation to eliminate the mass source errors, and then correct the pressures and corresponding velocity components.

7. If on the finest grid level, solve the equations for k, ϵ, and $\overline{u_i u_j}$, as the case may be.

8. Then solve the temperature equation.

These steps are repeated until convergence on the current finest grid. The multigrid process starts with the prolongation of converged solution on a coarse grid to the next finer grid. A fixed V-cycle full multigrid algorithm is then utilized with 10 iterations on the coarsest grid and 3 on intermediate grids and one iteration on the finest grid. Residuals of the momentum equations, as well as the cell-face mass flux equations are restricted onto coarser grids for smoothing. Since we employ the full approximation storage variant, which is applicable to a non-linear system [14], it is also necessary to restrict the velocities and the temperature. Restriction from fine to coarse grid is by 8-point averages. The difference between the restricted values and the smoothened solution on the coarse grid is prolongated onto the fine grid using trilinear interpolation. An ADI routine is employed to solve the final set of algebraic equations for all variables at all grid levels. The underlying algorithm is the tri-diagonal matrix algorithm (TDMA) which is known to be recursive, and would thus not normally be vectorizable. However, by a change in the data structure we can make all the internal loops of the ADI solver vectorizable on the Cray computers. Although we cannot remove the recursivity of the algorithm, the change in data structure ensures that all floating point operations are in vector form. Typical saving in total CPU time resulting from this change alone is of the order of 50% for an average vector length of 35.

The equations for turbulent quantities $\overline{u_i u_j}$ and ϵ are solved only on the current finest grid. Corresponding operators on coarser grids are calculated using restricted values for these quantities. However, the solution process on any fine grid is started with variable values prolongated from the converged solution on the immediate coarser grid.

In order to investigate the characteristics of jets in crossflow at low to medium R, we compute two cases with R = 0.5 and 2.0, respectively. These correspond to some of the cases for which Andreopoulos and Rodi [3] and Andreopoulos [4] present measured data of mean-flow and turbulent quantities.

RESULTS AND DISCUSSION

In the computations a non-uniform grid is utilized, with most points concentrated in the regions near the jet discharge and immediately downstream. The computational domain extends for 6 diameters from the symmetry axis to a free boundary, in the lateral direction, 11

diameters from the wall to a free boundary, in the vertical direction, and 22 diameters from the crossflow inlet to exit planes, in the streamwise direction. The 3-level multigrid scheme has (11,18,23) points on the coarsest level and (38,66,86) points on the finest level, in the y^1, y^2, y^3 directions, respectively. Figure 1 gives a perspective view of the finest grid distribution. Typically, 45 fine grid iterations are required for convergence to a normalized residual norm of 5×10^{-4}. With the overheads of the smoothing, restrictions and prolongations, this translates to about 120 total work units or 25 minutes of CPU time on the Cray 2 computer. It turns out that the time is evenly divided between the mean-flow and the turbulence field computations, which suggests that this is a good candidate for a dual-processor machine. The inlet plane for the crossflow is located 4D upstream ot the jet hole, and the outlet plane 18D. The other two boundaries are located far enough away as to have no influence on the jet.

Figure 2 compares the computed streamwise velocity contours, in the symmetry plane, for the two cases, and the normalized temperature contours are compared in Fig.3. Although both jets have a reverse flow region on their lee side, their regimes are quite different. The jet at low R has a very small core, beyond which it is quickly bent over by the crossflow and blends with the wall boundary layer. At higher R the jet has a core which is roughly 2D long, considerably shorter than the 4–6 D observed in free jets, and is bent over much more gradually. An characteristic feature of jet in crossflow is that the temperature and velocity contours are noncoincident. The core of the jet, indicated by the temperature field, is actually a region with high shear, and the peak streamwise velocity occurs not in the jet but in the crossflow, caused by the acceleration of the latter around the jet. Figure 4 compares the computations of the velocity field at R = 0.5 with measured data [3]. Turbulent quantities are compared in Fig. 5. The vertical velocity profiles along the symmetry plane show good agreement. It is notable that the flow reversal from upwards to downwards which occurs somewhere between 1D and 4D is predicted. This is associated with the downwash effect of the wake. Streamwise velocity profiles show good agreement between predicted and measured values. The lateral velocity in a longitudinal plane passing through the edge of the jet is also well predicted. Comparison of turbulent quantities in Fig. 5 indicates that the jet may have penetrated deeper into the crossflow than computed, which is surprising if one considers the correct prediction of the vertical velocity magnitudes. A plausible explanation is that the measurements may represent the averaged effect of large scale coherent structures which were observed near the edge of the jet but which the present turbulence model does not explicitly account for. In contrast, the comparisons at high R, show in Fig. 6 that we predict a higher penetration of the jet. The vertical velocity field is considerably overpredicted. Apart from this, the correct trends and magnitudes are predicted. Figure 7 shows similar comparisons for the Reynolds stresses. At 4D, the predicted turbulent kinetic energy levels are much higher than the measured values. The predictions indicate that there is significant dissipation downstream, whereas the experiments show little change in magnitudes so that by 6D and 10D predicted and measured levels are similar. That change is attributable to convection and diffusion. Sykes et al [5] also overpredicted the turbulence levels. It is believed that this is a result of the inadequacy of the dissipation equation in the region with

very high shear rates near the jet exit.

In Figs. 8–10 we examine the evolution of the vorticity field in cross-stream planes, (0D, 2D and 4D) as the flow progresses downstream. Figure 8 compares, at low and medium R, the lateral vorticity components. All along the wall there is a strong boundary layer vorticity which has a positive sense. At low R, a horse-shoe vortex is formed around the jet which then binds the jet fluid to the boundary layer. The picture is quite different at higher R. First, there is the formation of strong negative vorticity in the stagnation region along the front of the jet, which is convected above the jet by 2D and is almost completely diffused and dissipated by 4D. A horse-shoe vortex forms below it, which is quite strong at 2D, but considerably diminishes in strength by 4D. Between the horse-shoe vortex and the boundary-layer vortex is a weaker vortex with opposite sense in the wake of the jet. Figure 9 shows the vertical vorticity component. In both cases with low- and medium-R we have a similar pattern. There is a strong negative vorticity which emanates near the lip of the jet exit hole due to the expansion of the jet as it emerges. It is subsequently convected and dispersed by the jet–crossflow interaction. This is the dominant feature, though there is a vorticity pattern with the opposite sense near the symmetry plane. This pattern is also seen in Fig. 10 which shows the streamwise vorticity components. It is associated with the downwash effect of the wake and leads to a depression of the velocity and temperature contours near the symmetry axis. There is a strong negative vorticity produced by the acceleration of the crossflow as it bends around the jet. Some of this is then entrained into the jet through the wake region. The rest is wrapped around the jet and is dispersed further downstream. At low R, there is a much smaller wake region, so this process takes place within a short distance.

CONCLUDING REMARKS

The present mathematical procedure predicts correctly the basic features of turbulent jets in crossflow at low to medium jet to crossflow velocity ratio. There is some quantitative discrepancy between model results and experimental data which is presumed to be partly due to model deficiency and inadequacies in the measurement techniques. Further, boundary conditions at the jet discharge plane which are difficult to specify because of the crossflow interaction have significant effects on the computed flow field. They are rarely ever measured in sufficient detail. The differences in the jet-crossflow interaction at low to medium R are examined through the evolution of the vorticity field.

ACKNOWLEDGEMENT

8

REFERENCES

1. Y. Kamotani, and I. Greber, Experiments on a turbulent jet in crossflow, *AIAA J.* **10**, 1425–1429 (1972).

2. J.F. Foss, Interaction region phenomena for the jet in a cross-flow problem, Rep. SFB 80/E/161, University of Karlsruhe, (1980).

3. J. Andreopoulos, and W. Rodi, An experimental investigation of jets in a crossflow *J. Fluid Mech.* **138**, 93–127 (1984).

4. J. Andreopoulos, On the structure of jets in a crossflow, *J. Fluid Mech.* **157**, 163–197 (1985).

5. R.I. Sykes, W.S. Lewellen, and S.F. Parker, On the vorticity dynamics of a turbulent jet in a crossflow, *J. Fluid Mech.* **168**, 393–413 (1986).

6. B.E. Launder, G.J. Reece, and W. Rodi, Progress in the development of a Reynolds stress turbulence closure. *J. Fluid Mech.* **68**, 537–566 (1975).

7. A.O. Demuren, and W. Rodi, Calculation of turbulence-driven secondary motion in non-circular ducts *J. Fluid Mech.* **140**, 189–222 (1984).

8. A.T. Degani, and, J.D.A. Walker, Computation of three-dimensional turbulent boundary layers with heat transfer in a plane of symmetry using embedded wall-layer functions, AIAA paper no. AIAA-90-0307, (1990).

9. A.O. Demuren, and, W. Rodi, Side discharges into open channel: mathematical model, *ASCE, J. Hyd. Engg.* **109**, No. 12, 1707–1722 (1983).

10. S.V. Patankar, and, D.B. Spalding, A calculation procedure for heat, mass and momentum transfer in 3-D parabolic flows," *Int. J. of Heat and Mass Transfer* **15**, 1787–1806 (1972).

11. J.P. van Doormaal, and B.D. Raithby, Enhancements of the SIMPLE method for predicting incompressible fluid flows, *Numer. Heat Trans.* **7**, 147–163 (1984).

12. R.I. Issa, Solution of implicitly discretized fluid flow equations by operator-splitting, *J. Comp. Phys.* **62**, 40–65 (1985).

13. G.J. Shaw, and, S. Sivaloganathan, On the smoothing properties of the SIMPLE pressure-correction algorithm, *Int. J. Num. Meth. Fluids* **8**, 441-461 (1988).

14. A. Brandt, Multi-level adaptive solutions to boundary-value problems, *Math. of Comp.* **31**, 330-390 (1977).

15. A.O. Demuren, Application of multi-grid methods for solving the Navier-Stokes equations, *Proc. Inst. Mech. Engrs.* **203**, 255–265 (1989).

16. S.P. Vanka, Block-implicit multi-grid solution of Navier-Stokes equations in primitive variables, *J. Comput. Phys.* **65**, 138–158 (1986).

17. M. Peric, A finite volume method for the prediction of three dimensional fluid flow in complex ducts, Ph.D. Thesis, (University of London, 1985).
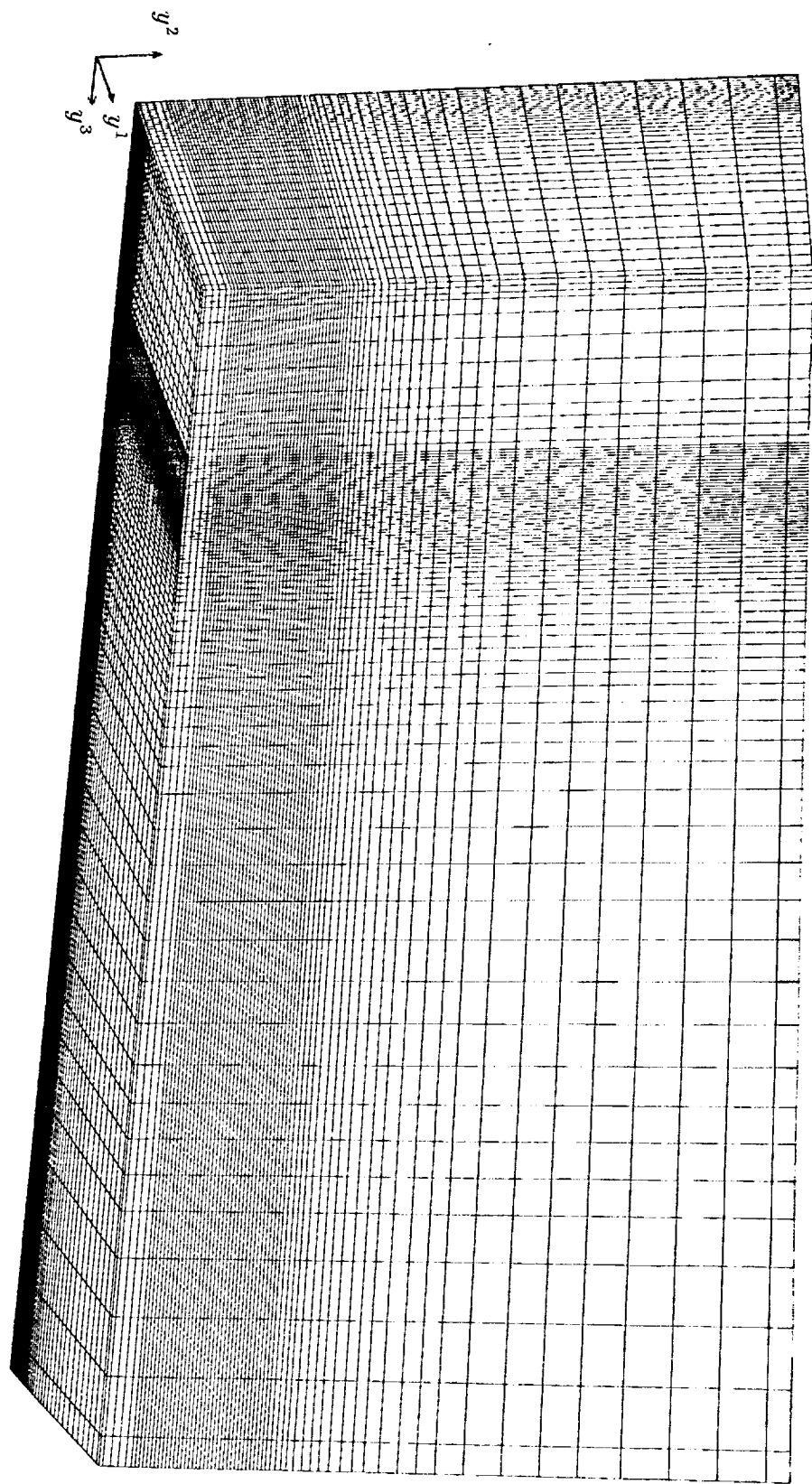
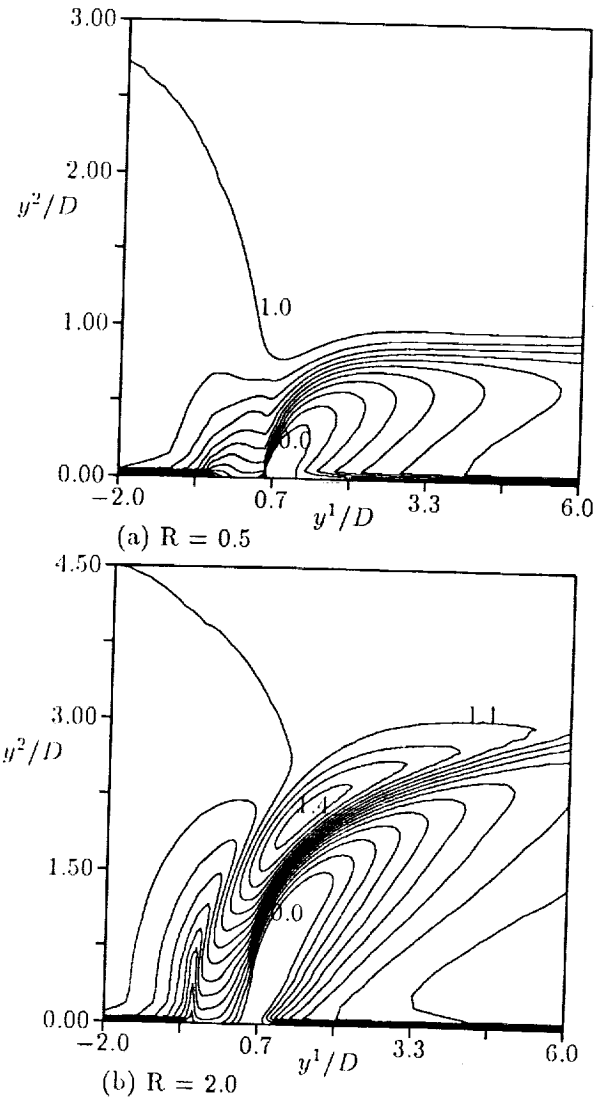FIG. 1. Computational grid on finest level

11

3.00

y^2/D

2.00

1.00

1.0

0.0

0.00

−2.0   0.7   3.3   6.0
y^1/D

(a) R = 0.5

4.50

y^2/D

3.00

1.1

1.50

0.0

0.00

−2.0   0.7   3.3   6.0
y^1/D

(b) R = 2.0

FIG. 2. Streamwise velocity contours, U_3/U_∞ in symmetry plane
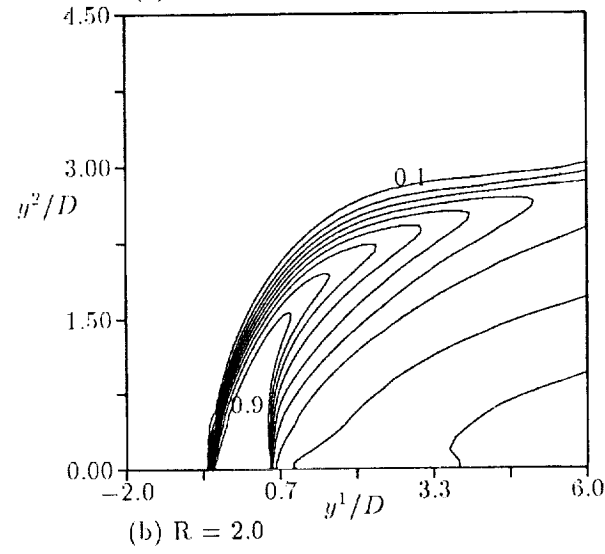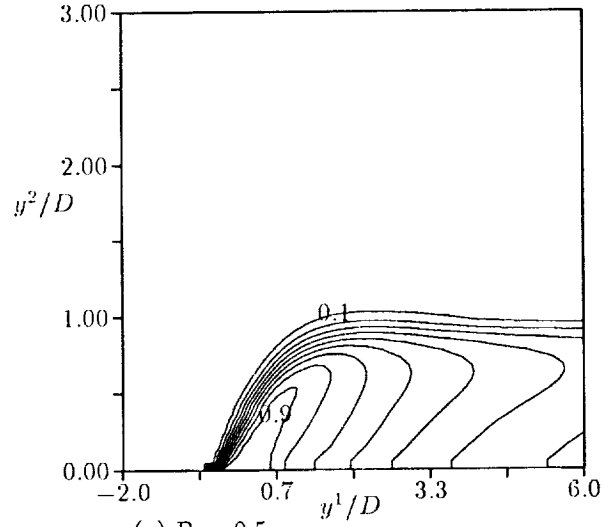
FIG. 3. Normalized temperature contours, $(T - T_\infty)/(T_j - T_\infty)$ in symmetry plane

13
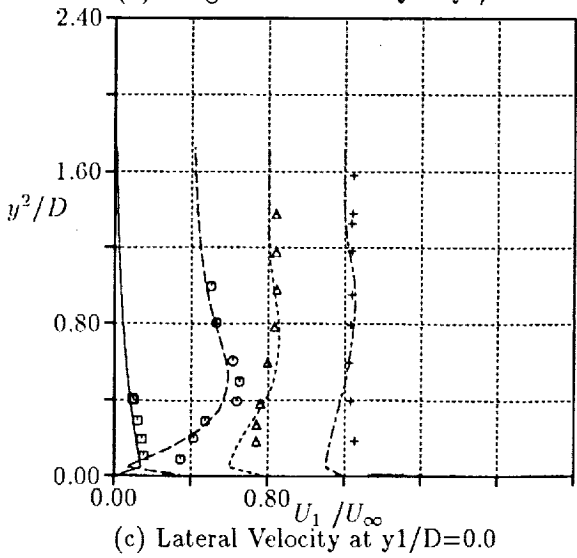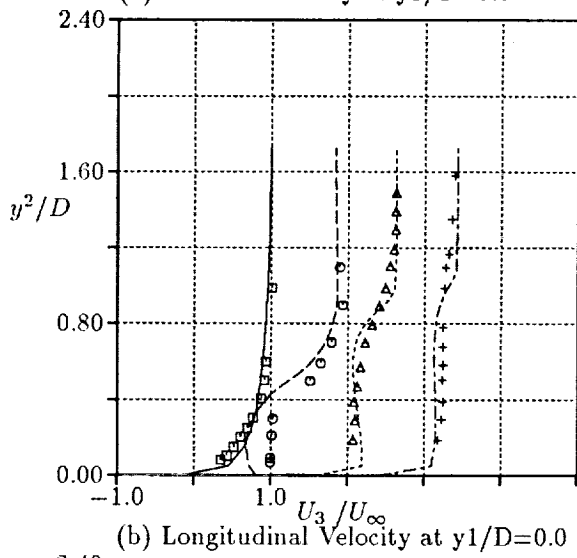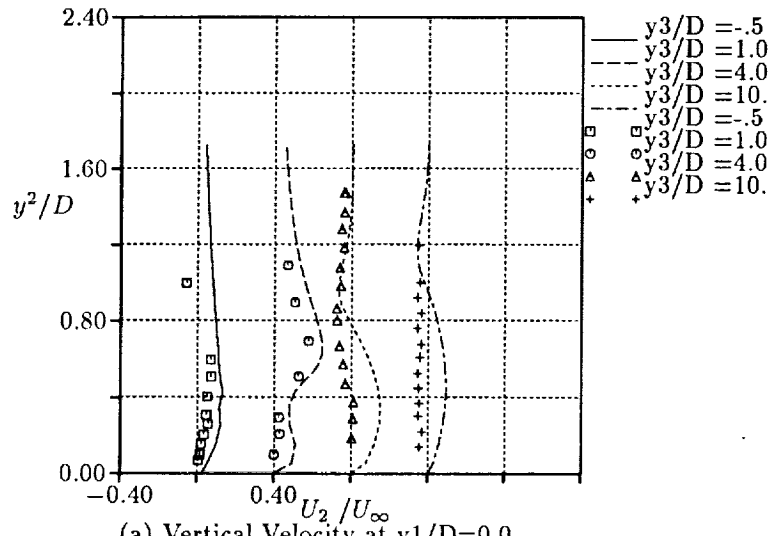
FIG. 4. Comparison of computations (lines) and experimental
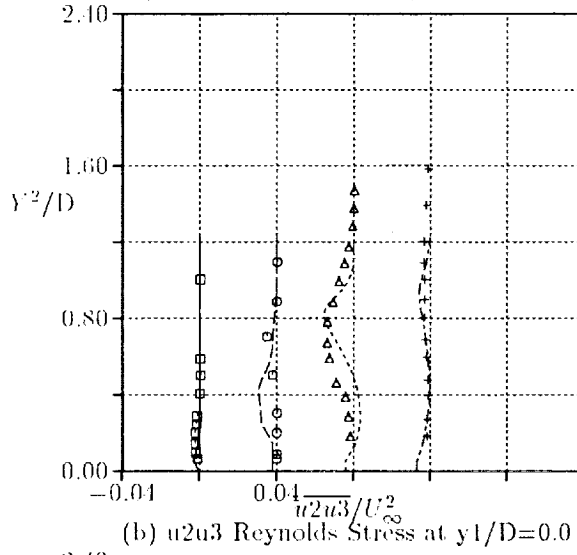data (symbols) [3], R=0.5 :velocity field

2.40
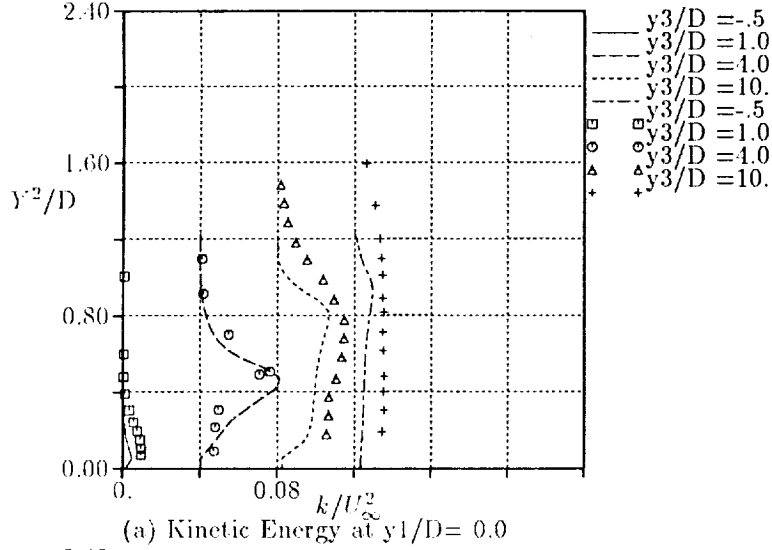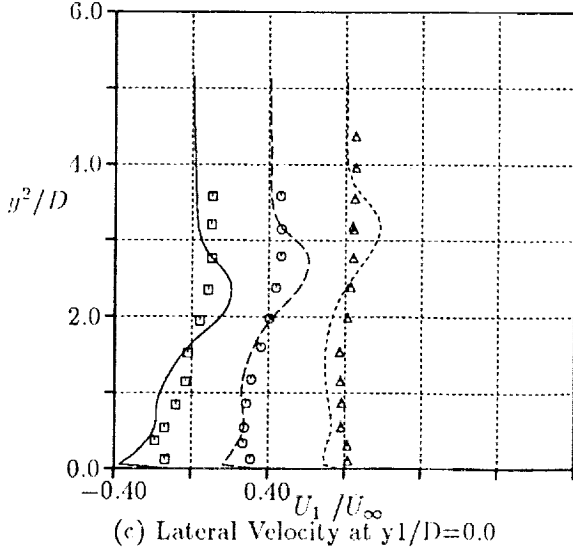
y3/D =−.5
y3/D =1.0
y3/D =4.0
y3/D =10.
y3/D =−.5
y3/D =1.0
y3/D =4.0
y3/D =10.

Y^2/D

1.60

0.80

0.00

0.   0.08 k/U_∞^2

(a) Kinetic Energy at y1/D= 0.0

2.40

Y^2/D

1.60

0.80

0.00

−0.04   0.04 $\overline{u2u3}/U_\infty^2$

(b) u2u3 Reynolds Stress at y1/D=0.0

2.40

Y^2/D

1.60

0.80

0.00

−0.04   0.04 $\overline{u1u3}/U_\infty^2$

(c) u1u3 Reynolds Stress at y1/D= 0.5
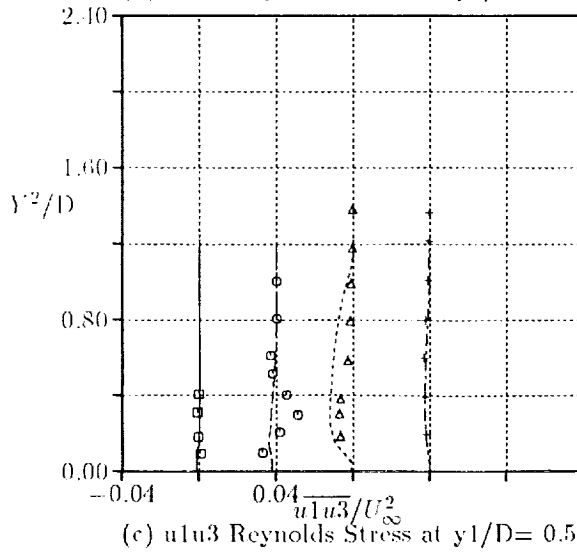
FIG. 5. Comparison of computations (lines) and experimental
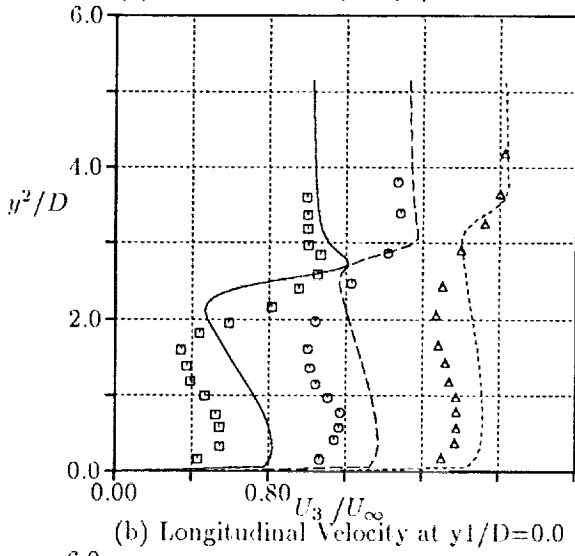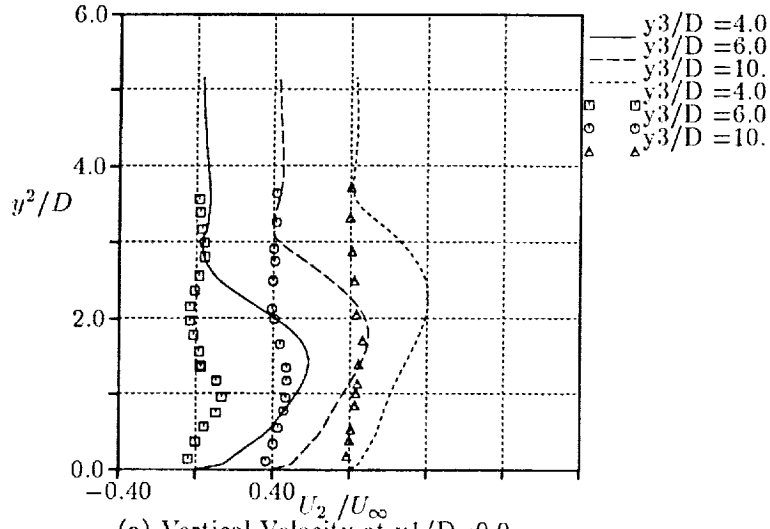data (symbols) [3], R−0.5 :turbulence field

15

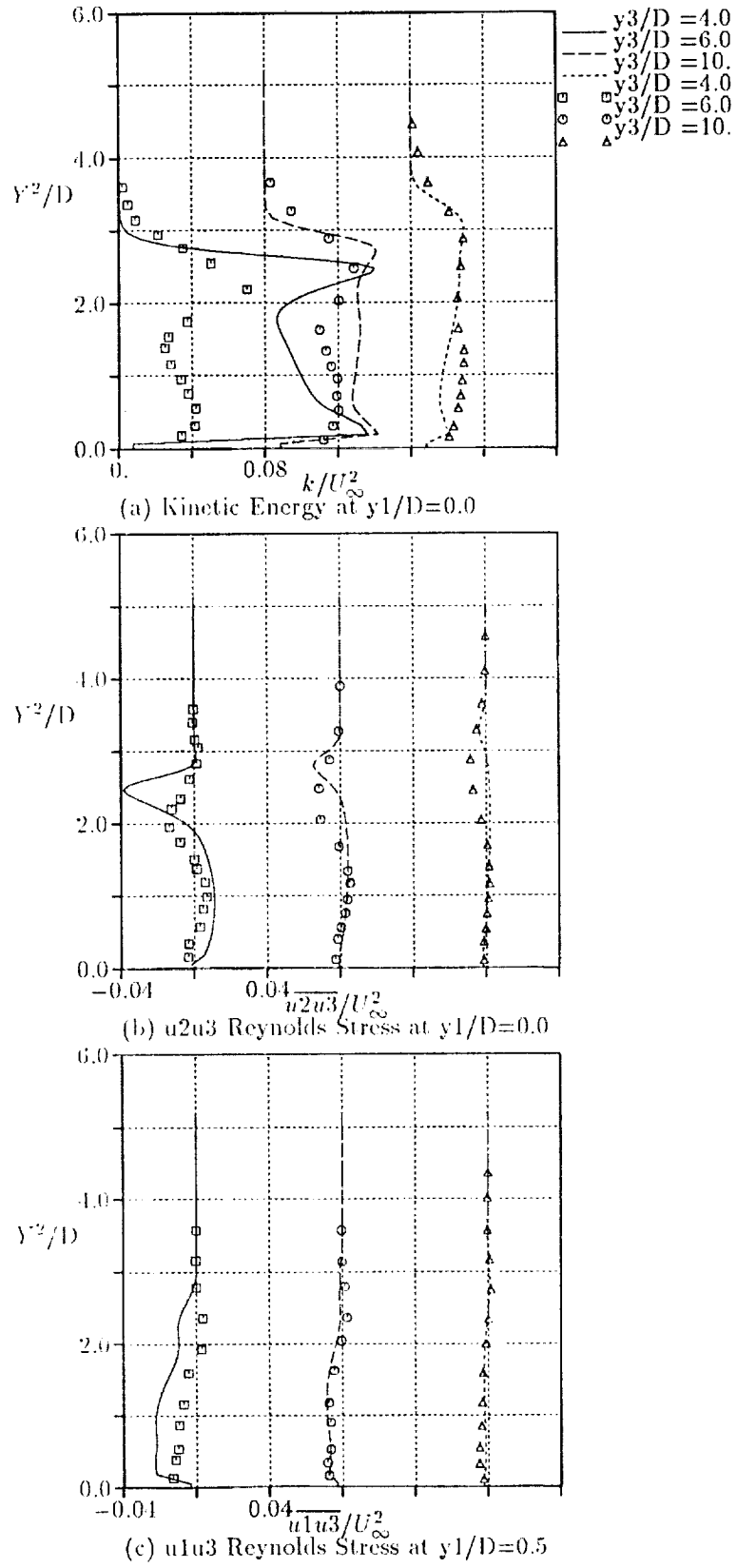FIG. 6. Comparison of computations (lines) and experimental data (symbols) [3], R=2.0 :velocity field

6.0

y3/D =4.0
y3/D =6.0
y3/D =10.
y3/D =4.0
y3/D =6.0
y3/D =10.

4.0

$Y2/D$

2.0

0.0

0.   0.08 k/U_∞^2

(a) Kinetic Energy at y1/D=0.0

6.0

4.0

$Y2/D$

2.0

0.0

-0.04   0.04 $\overline{u2u3}/U_\infty^2$

(b) u2u3 Reynolds Stress at y1/D=0.0

6.0

4.0

$Y2/D$

2.0

0.0

-0.04   0.04 $\overline{u1u3}/U_\infty^2$

(c) u1u3 Reynolds Stress at y1/D=0.5

FIG. 7. Comparison of computations (lines) and experimental data (symbols) [3], R=2.0 :turbulence field
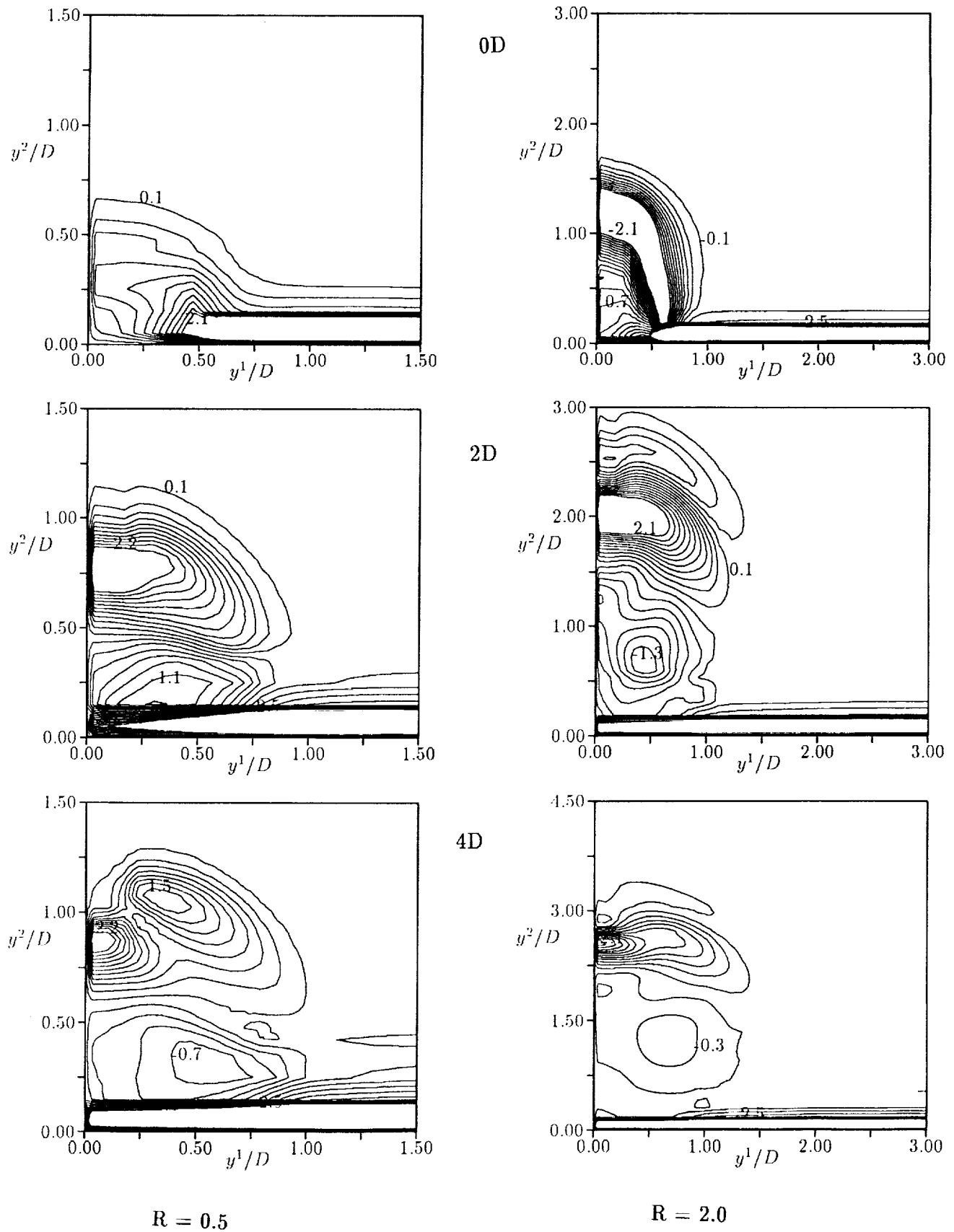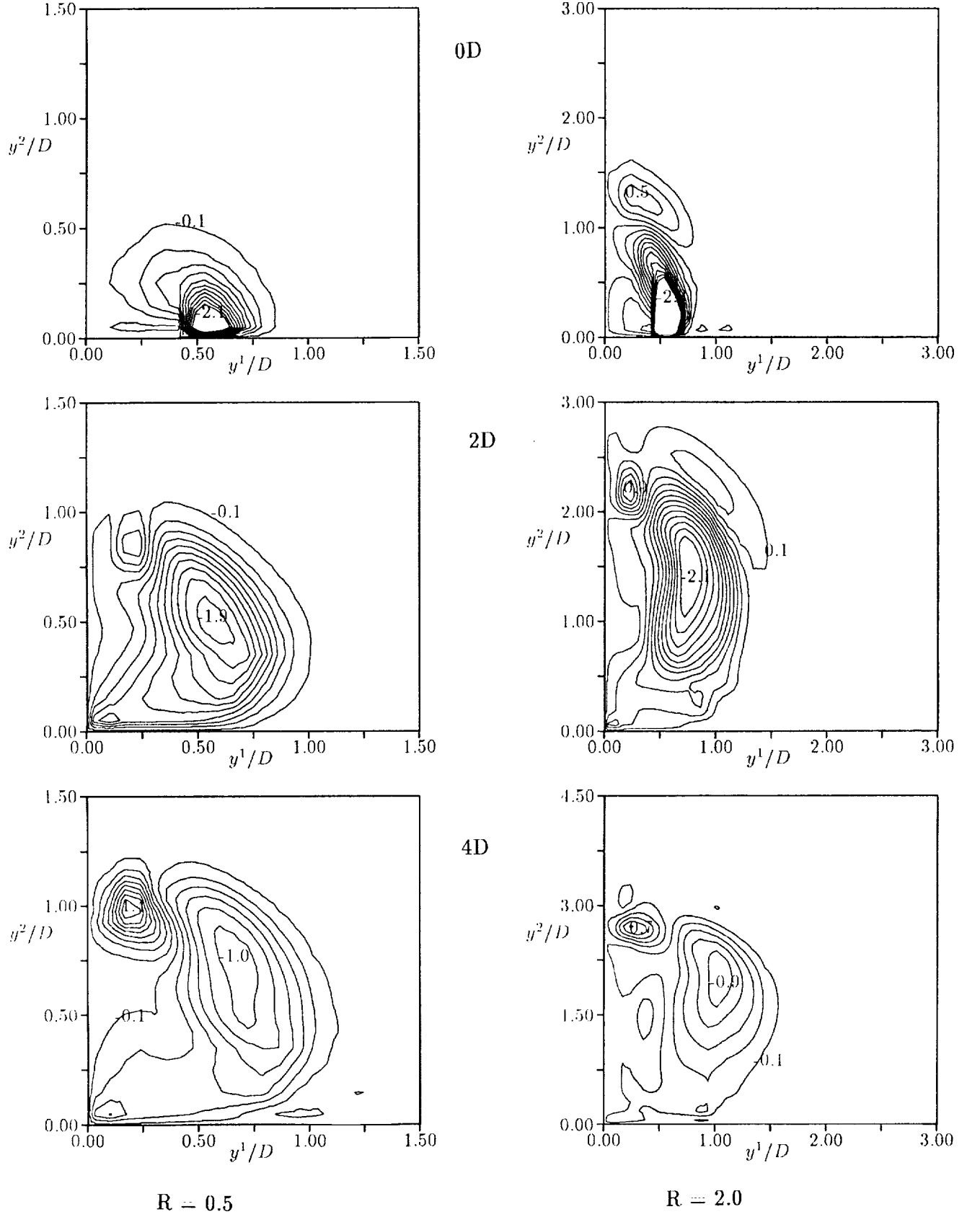
17

0D

2D

4D

R = 0.5

R = 2.0

FIG. 8. Lateral vorticity, $\Omega_1/(U_\infty D)$ contours in cross-stream planes

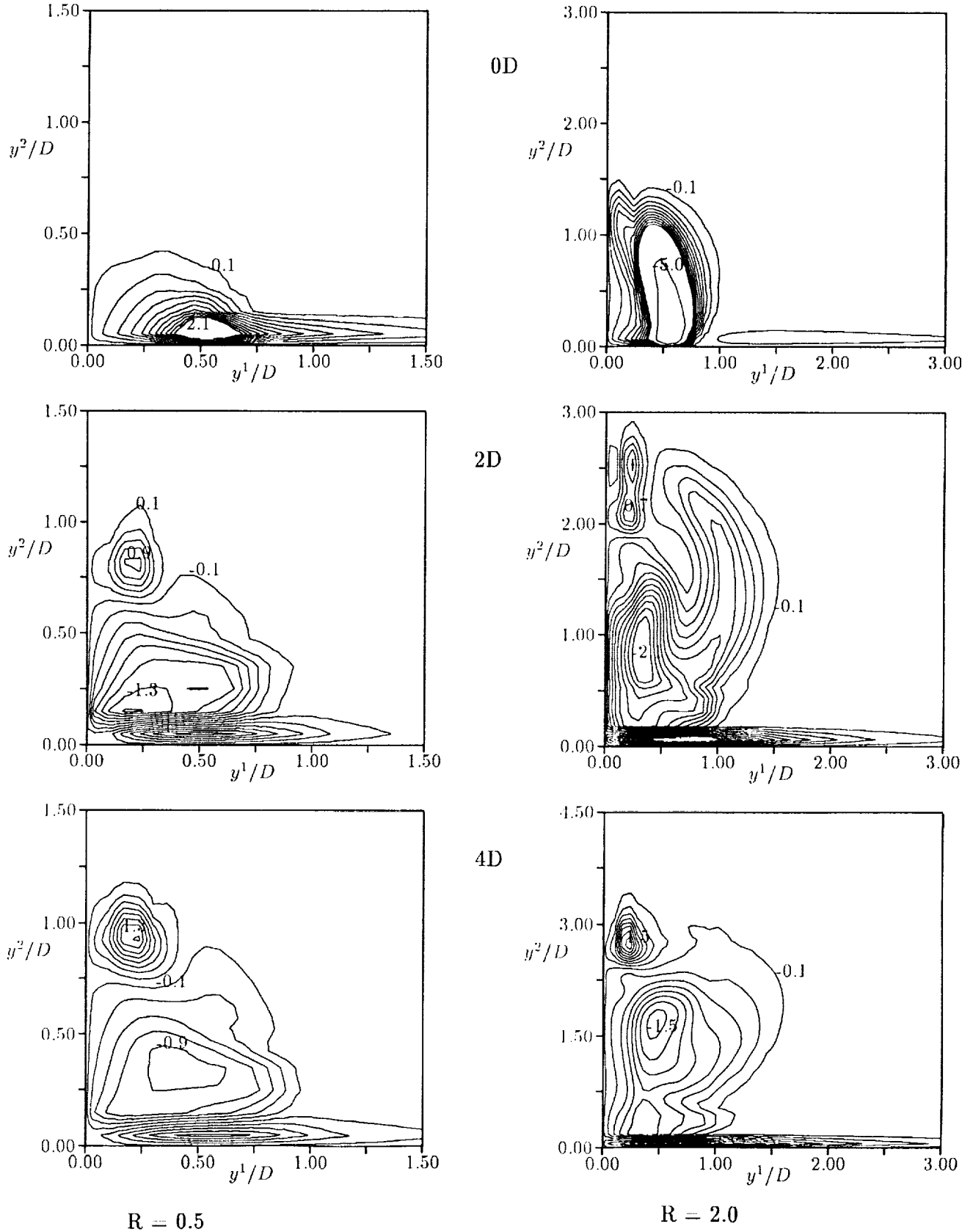FIG. 9. Vertical vorticity, $\Omega_2/(U_\infty D)$ contours in cross-stream planes

0D

2D

4D

R = 0.5

R = 2.0

FIG. 10. Longitudinal vorticity, $\Omega_3/(U_\infty D)$ contours in cross-stream planes

20

NASA
National Aeronautics and
Space Administration

Report Documentation Page

1. Report No. NASA TM-104337 ICOMP-91-05	2. Government Accession No.	3. Recipient's Catalog No.

4. Title and Subtitle		5. Report Date
Characteristics of 3D Turbulent Jets in Crossflow		April 1991
		6. Performing Organization Code

7. Author(s)	8. Performing Organization Report No.
A.O. Demuren	E-6106
	10. Work Unit No. 505-62-21

9. Performing Organization Name and Address	
National Aeronautics and Space Administration Lewis Research Center Cleveland, Ohio 44135-3191	11. Contract or Grant No.
	13. Type of Report and Period Covered
12. Sponsoring Agency Name and Address	Technical Memorandum
National Aeronautics and Space Administration Washington, D.C. 20546-0001	14. Sponsoring Agency Code

16. Abstract

Three-dimensional turbulent jets in crossflow at low to medium jet-to-crossflow velocity ratios are computed with a finite-volume numerical procedure which utilizes a second-moment closure model to approximate the Reynolds stresses. A multigrid method is used to accelerate the convergence rate of the procedure. Comparison of the computations to measured data show good qualitative agreement. All trends are correctly predicted, though there is some uncertainty on the height of penetration of the jet. The evolution of the vorticity field is used to explore the jet-crossflow interaction.

17. Key Words (Suggested by Author(s))	18. Distribution Statement
Jets Reynolds stress Turbulence models Computational fluid dynamics	Unclassified - Unlimited Subject Category 34

19. Security Classif. (of the report)	20. Security Classif. (of this page)	21. No. of pages	22. Price*
Unclassified	Unclassified	22	A03